



Phase decomposition and electrochemical properties of single phase $\text{La}_{1.6}\text{Mg}_{0.4}\text{Ni}_7$ alloy

Lu Zhang^b, Shumin Han^{a, b, *}, Da Han^c, Yuan Li^b, Xin Zhao^b, Jingjing Liu^b

^a State Key Laboratory of Metastable Materials Science and Technology, Yanshan University, Qinhuangdao 066004, PR China

^b College of Environmental and Chemical Engineering, Yanshan University, Qinhuangdao 066004, PR China

^c Department of Chemistry and Department of Physiology and Function Genomics, Center for Research at the Bio/Nano Interface, Shands Cancer Center and UF Genetics Institute, University of Florida, Gainesville, FL 32611-7200, United States

HIGHLIGHTS

- Ce_2Ni_7 -type single phase $\text{La}_{1.6}\text{Mg}_{0.4}\text{Ni}_7$ alloy is obtained by annealing treatment.
- Cell volume change rate of $[\text{La}_{1.22}\text{Mg}_{0.78}\text{Ni}_4]$ is larger than of $[\text{LaNi}_5]$ (I and II).
- Ce_2Ni_7 -type phase decomposes into amorphous La and Mg, nano Ni and LaNi_5 .
- Phase decomposition contributes to decrease of discharge capacity.
- Single phase alloy electrode has superior discharge capacity and cycling stability.

ARTICLE INFO

Article history:

Received 6 March 2014

Received in revised form

27 May 2014

Accepted 16 June 2014

Available online 24 June 2014

Keywords:

Metal hydride alloy

Single phase

Hydrogenation/dehydrogenation

Phase decomposition mechanism

Electrochemical properties

ABSTRACT

The Ce_2Ni_7 -type (hexagonal, 2H) single phase $\text{La}_{1.6}\text{Mg}_{0.4}\text{Ni}_7$ alloy has been obtained by annealing the induction melting as-cast sample at 1223 K for 12 h. The relationship between phase structural stability and volume change rate of the three kinds of slabs in Ce_2Ni_7 -type structure is studied. It is found that the volume change rate of Mg-containing $[\text{La}_{1.22}\text{Mg}_{0.78}\text{Ni}_4]$ slab after hydrogenation/dehydrogenation is larger than that of $[\text{LaNi}_5]$ I (outer) and $[\text{LaNi}_5]$ II (inner) slabs, and the consecutive cell volume change of $[\text{La}_{1.22}\text{Mg}_{0.78}\text{Ni}_4]$ slab ultimately results in the decomposition of Ce_2Ni_7 -type phase $\text{La}_{1.6}\text{Mg}_{0.4}\text{Ni}_7$ to amorphous La and Mg phases, nanocrystalline Ni, and CaCu_5 -type LaNi_5 phases, as well as the reduction of electrochemical discharge capacity. Electrochemical studies show that the single phase alloy electrode possesses good discharge capacity (400 mAh g^{-1}) and cycling stability (84.2% after 100 cycles). The improvement in phase structure stability and the cycling stability of the superlattice structure alloys can be achieved by inhibiting the significant volume change of Mg-containing slabs during hydrogenation/dehydrogenation.

© 2014 Elsevier B.V. All rights reserved.

1. Introduction

The intermetallic La–Mg–Ni-based alloys with superlattice structures have been applied as hydrogen storage materials because of their superior hydrogen storage properties, i.e., 25% higher than that of the commercially available LaNi_5 alloys [1–6]. These La–Mg–Ni-based alloys composed of slabs with $[\text{AB}_5]$ and $[\text{A}_2\text{B}_4]$ slabs stack along the *c* axis and form various AB_x -type phase structures, where $x = (5n + 4)/(n + 2)$ and *n* is an integer ($n = 1, 2, \dots$), with A = La, Mg and B = Ni [7–11].

Among them, $\text{AB}_{3.5}$ -type $(\text{La}, \text{Mg})_2\text{Ni}_7$ ($n = 2$) is known to crystallize into two structures: a hexagonal 2H-type structure (space group $\text{P6}_3/\text{mmc}$, no. 194) with the stacking of $2(n \times [\text{AB}_5] + [\text{A}_2\text{B}_4])$ at high temperatures and a rhombohedra 3R-type structure (space group $\text{R}\bar{3}\text{m}$, no. 166) with the stacking of $3(n \times [\text{AB}_5] + [\text{A}_2\text{B}_4])$ at relatively lower temperatures. The corresponding 2H- and 3R-type structures of $(\text{La}, \text{Mg})_2\text{Ni}_7$ mentioned above are Ce_2Ni_7 - and Gd_2Co_7 -type in X-ray crystallography, respectively. The structural differences between the 2H- and 3R-type variants exist only in the stacking modes of $[\text{A}_2\text{B}_4]$ slabs, including hexagonal MgZn_2 - (C14) and cubic MgCu_2 -type (C15) Laves phases.

Recent studies show that the cycling stability of $\text{AB}_{3.5}$ -type $(\text{La}, \text{Mg})_2\text{Ni}_7$ alloys is superior to that of AB_3 -type $(\text{La}, \text{Mg})\text{Ni}_3$ alloys. To reveal the reasons, people have focused on studying the crystal

* Corresponding author. College of Environmental and Chemical Engineering, Yanshan University, Qinhuangdao 066004, PR China. Tel./fax: +86 335 8074648.

E-mail addresses: hanshm@ysu.edu.cn, liyuan@ysu.edu.cn (S. Han).

structures and electrochemical properties of AB_{3.5}-type (La,Mg)₂Ni₇ alloys. However, most of the obtained AB_{3.5}-type (La,Mg)₂Ni₇ alloys are with multiphase structures because of the difficulty in preparing single phase structures in regards to their narrow composition in La–Ni system [12], which hinders the further studies in structures of these alloys. Therefore, research towards creating single-phase structure alloys has been carried out intensively. Zhang et al. made a double-phase 2H- and 3R-type La_{1.5}Mg_{0.5}Ni₇ by annealing at 1173 K with the corresponding abundance of 43% and 57% for these two structures. As a result of the double-phase structure, the maximum discharge capacity and capacity retention ratio after 150 cycles was found to be up to 389 mAh g⁻¹ and 82.0% [13]. Afterwards, Ce₂Ni₇-type (2H-type) phase La_{1.5}Mg_{0.5}Ni₇ was obtained by annealing the as-cast sample at 1123 K, but still accompanied with 3.2 wt.% CaCu₅-type LaNi₅ phase [14]. In addition, Denys et al. studied the influence of magnesium on the crystal structure and the hydrogenation behavior of Ce₂Ni₇-type single phase La_{1.5}Mg_{0.5}Ni₇ by sintering LaNi_{4.67} and Mg powder with La₂Ni₇ [15]. Besides, how the presence of Mg affects the possible structural changes and the hydrogen capacity of an alloy was also investigated by determining the hydrogen site configurations in hydrides/deuterides of single phase La_{1.63}Mg_{0.37}Ni₇ and La_{1.64}Mg_{0.36}Ni₇ [16]. Although, the single phase Ce₂Ni₇-type (La,Mg)₂Ni₇ alloy has been prepared and studied, the relationship between the cycling stability and its structure change, as well as the structural stability of the intrinsic stacking slabs is unclear. It has been found that, in PuNi₃-type LaNi₃ alloys, the reduction of its irreversible capacity is due to immediately hydrogen-induced amorphization (HIA) in the [A₂B₄] slabs [17]. Besides, the HIA is a character of Laves (C14 or C15) phase that the phase transforms to amorphous state after hydrogen absorption [18,19]. For Ce₂Ni₇-type phase of which the [A₂B₄] slabs are C14 Laves structure, attenuation may also related to the [A₂B₄] slabs, but investigation on this aspect is still a vacancy. Therefore, the primary goal of our study is to elucidate the structural changes of the intrinsic stacking slabs of [AB₅] and [A₂B₄] slabs in a single phase Ce₂Ni₇-type (La,Mg)₂Ni₇ after hydrogen absorption/desorption processes and the relationship between the phase structural stability and the structural changes of the slabs, as well as the electrochemical properties in the single phase Ce₂Ni₇-type (La,Mg)₂Ni₇.

Sintering and induction melting synthesis routes are widely applied to obtain homogeneous single phase of La–Mg–Ni-based alloys. Sintering method, however, often takes its toll on the Mg content that usually makes the desired alloys with many porous holes and results in the decrease in inferior electrochemical cycling stability [20]. Although the alloys obtained by the induction melting can effectively diminish the defects, the generation of multiphase structures is one of the main disadvantages of the induction melting method in the process of making a single phase. Therefore, annealing is useful to eliminate the impurity phases via a peritectic reaction when adopting the induction melting route, and obtain a homogeneous single phase structure alloy.

Based on the discuss above, we have prepared a Ce₂Ni₇-type single phase La_{1.6}Mg_{0.4}Ni₇ alloy by annealing the induction melting sample and obtained stable experimental conditions of making the single phase alloy. In this study, we present the crystal structures, gas solid hydrogen storage behaviors and electrochemical properties of the Ce₂Ni₇-type single phase La_{1.6}Mg_{0.4}Ni₇ alloy. In addition, the structural parameters and volumetric expansions of the unit [AB₅] and [A₂B₄] slabs after hydrogen absorption/desorption were analyzed. Specifically, a phase decomposition phenomenon of the Ce₂Ni₇-type single phase alloy after several cycles of hydrogen absorption/desorption was found and the mechanism was subsequently studied to theoretically explain the attenuation of the electrochemical capacity of AB_{3.5}-type La–Mg–Ni-based alloys.

2. Experiment

La_{1.6}Mg_{0.4}Ni₇ alloy was prepared by induction melting constituent metals La, Mg and Ni with a purity of 99.5%. The blocky as-cast alloys (~10 g) were wrapped in nickel foil, placed in a furnace and then heated up to 1123, 1173, and 1223 K for 12 h (heating rate 4 °C min⁻¹ below 600 °C and 1 °C min⁻¹ above 600 °C) under 0.04 MPa argon atmosphere, respectively. A slight excess of Mg was used to compensate for the evaporation during the annealing procedure and to reduce the loss of Mg. The chemical analysis of the annealed samples was conducted using inductively coupled plasma (ICP) analyzers.

Alloys were crushed mechanically into particles (<400 mesh) for X-ray diffraction (XRD) measurements with a Rigaku D/Max-2500/PC X-ray diffractometer (Cu K α radiation). The pattern of the alloy annealing at 1223 K was recorded over the range from 10° to 80° in 2 θ by a step of 1° min⁻¹. Then the collected data was analyzed by the Rietveld method using RIETICA software [21]. The degree of the refinement is judged by S : $S = R_{wp}/R_e$, where R_{wp} is the residue of the weighted pattern and R_e is the statistically expected residue value. Morphology of the alloys was observed by S-3400 scanning electron microscopy (SEM) connecting with energy dispersive spectrometer (EDS). Specimens for transmission electron microscopy (TEM) were prepared by mechanical lapping under alcohol then processed by ultrasounding for 30 min. TEM were performed on JEM-2010 with energy-dispersive X-ray (EDX) operating at 20.0 kV to determine the chemical composition of the samples.

The samples for the pressure-composition (P – C) isotherm measurement were firstly activated by repeatedly hydriding-dehydriding the alloys at room temperature for four times. Then the alloys were heated in a vacuum at 473 K at 2.0 MPa for 3 h and vacuumed at room temperature for 3 h in a stainless-steel container. The P – C isotherms were measured using Sieverts' method at 298, 323, and 348 K.

A testing electrode was prepared by pressing a mixture of 0.15 g alloy powder and 0.75 g nickel powder into a pellet of 10 mm under 15 MPa. The pellet was wrapped into nickel foam, pressed under 10 MPa, and then welded to a nickel strap. Electrochemical measurements were performed at 298 K in a tri-electrode system consisting of MH electrode as the working electrode, Ni(OH)₂/NiOOH electrode as the counter electrode, Hg/HgO electrode as the reference electrode and a 30% KOH solution as the electrolyte. The charge/discharge tests followed the procedures reported in the literature [22].

3. Results and discussion

3.1. Crystal structures

Fig. 1 shows the XRD patterns of the as-cast and annealed samples under different annealing temperatures for 12 h. The as-cast alloy pattern includes CaCu₅-type LaNi₅, Ce₂Ni₇- and Gd₂Co₇-type (La,Mg)₂Ni₇, and Ce₅Co₁₉-type (La,Mg)₄Ni₁₉ phases. CaCu₅-type phase disappears after the annealing operation at 1123 K. Similarly, with temperature increasing to 1173 and 1223 K, Ce₅Co₁₉- and Gd₂Co₇-type phases disappear respectively, and the single phase Ce₂Ni₇-type La_{1.6}Mg_{0.4}Ni₇ is subsequently obtained at 1223 K. This result suggests that the crystal growth temperature of the Ce₂Ni₇-type single phase La_{1.6}Mg_{0.4}Ni₇ alloy is 1223 K, 30 K lower than the binary La₂Ni₇ alloy, indicating that higher temperature is favorable to element diffusions between close phases to form single phase with high crystallinity.

Fig. 2 shows the Rietveld refinement of the La_{1.6}Mg_{0.4}Ni₇ alloy annealed at 1223 K. The refined atomic coordinates and occupation

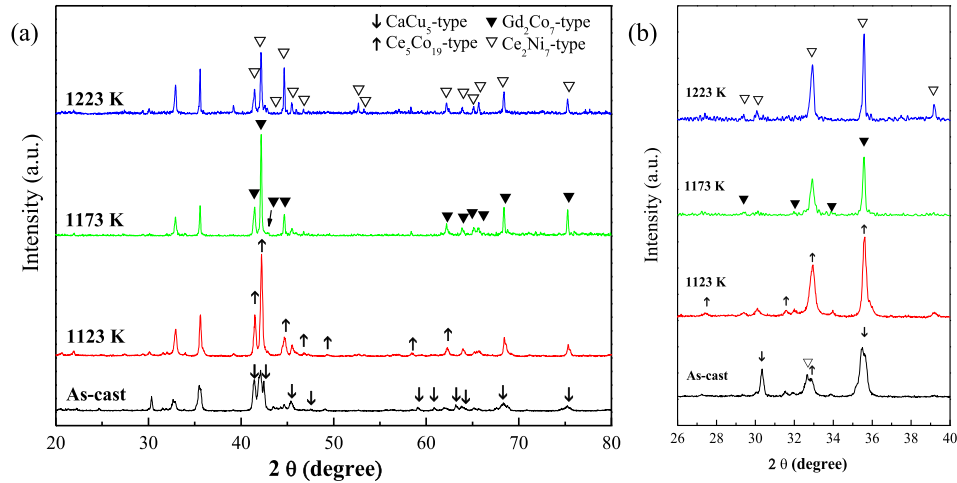


Fig. 1. Evolution of the XRD patterns for the as-cast and annealed $\text{La}_{1.6}\text{Mg}_{0.4}\text{Ni}_7$ alloys: (a) in the 2θ range of $20\text{--}80^\circ$, (b) zoom of (a) in the 2θ range of $26\text{--}40^\circ$ in order to show the evolution of the diffraction peaks.

numbers of Ce_2Ni_7 -type structure mode of the $\text{La}_{1.6}\text{Mg}_{0.4}\text{Ni}_7$ alloy is listed in Table 1, with the stacking structure shown in Fig. 3. The isolation of $[\text{A}_2\text{B}_4]$ slab from $[\text{AB}_5]$ slab is based on Ni5 sites, and separations of the two $[\text{AB}_5]$ slabs are decided by Ni4 sites (as shown in Fig. 3(b)). Two fifths of La1 sites are preferentially occupied by Mg atoms, but neither La2 sites nor Ni sites are filled with Mg atoms, indicating that Mg atoms occupy La1 sites in the $[\text{A}_2\text{B}_4]$ slab, as reported previously [14,15]. The refined lattice parameters are shown in Table 2 with $a = 5.0409 \text{ \AA}$, $c = 24.290 \text{ \AA}$ and $V = 534.49 \text{ \AA}^3$. Compared to pure La_2Ni_7 , the volume contraction ratios of unit cell parameters with the introduction of Mg for $\text{La}_{1.6}\text{Mg}_{0.4}\text{Ni}_7$ are: $\Delta a/a = -0.34\%$, $\Delta c/c = -1.7\%$ and $\Delta V/V = -2.4\%$. The volume of $[\text{A}_2\text{B}_4]$ slab in respect to the composition of $\text{La}_{1.22}\text{Mg}_{0.78}\text{Ni}_4$, significantly reduces by 5.9%, but only with minor change of 0.4% in $[\text{AB}_5]$ slabs. The occupation of Mg (1.602 \AA) in La (1.877 \AA) site ($4f_1$) shortens the La–La inter-atomic distance in $[\text{A}_2\text{B}_4]$ slab, but almost remains constant in the basal plane which is contiguous with $[\text{AB}_5]$ slab, leading to an anisotropic slab parameter reduction and a fifteen times volume contraction of $[\text{A}_2\text{B}_4]$ slab compared to $[\text{AB}_5]$ slabs. With the increasing substitution amount

of Mg to La site, the parameters of a , c , V , $V_{\text{A}_2\text{B}_4}$ and V_{AB_5} diminish, resulting in a reverse correlation between the unit cell and the substitution amount of Mg to La.

Fig. 4(a) and (b) show the SEM-EDS analysis of the $\text{La}_{1.6}\text{Mg}_{0.4}\text{Ni}_7$ alloy. It can be seen in Fig. 4(a) that there is only one area originally exhibiting single-phase structure with minor amount of bright dots, which are determined to be $\text{La}_{0.9}\text{Mg}_{0.1}\text{Ni}_{4.19}\text{O}_{0.46}$. These bright

Table 1

Atomic coordinates and occupation numbers for Ce_2Ni_7 -type structure mode of $\text{La}_{1.6}\text{Mg}_{0.4}\text{Ni}_7$ alloy.

Atom	Wyck.	x	y	z	Occup.
La1	4f	1/3	2/3	0.02575	0.61
Mg	4f	1/3	2/3	0.02575	0.39
La2	4f	1/3	2/3	0.17042	1
Ni1	2a	0	0	0	1
Ni2	4e	0	0	0.16741	1
Ni3	4f	1/3	2/3	0.83363	1
Ni4	6h	0.8337	2x	1/4	1
Ni5	12k	0.8333	2x	0.08483	1

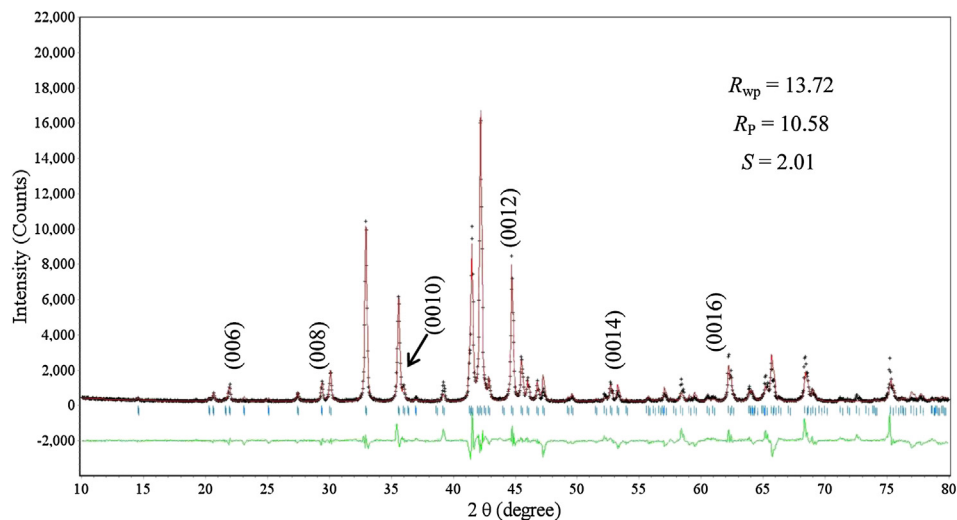


Fig. 2. Rietveld refinement of XRD pattern for $\text{La}_{1.6}\text{Mg}_{0.4}\text{Ni}_7$ alloy annealed at 1223 K. Vertical bar below the pattern show the positions of the reflection peaks of the Ce_2Ni_7 -type structure.

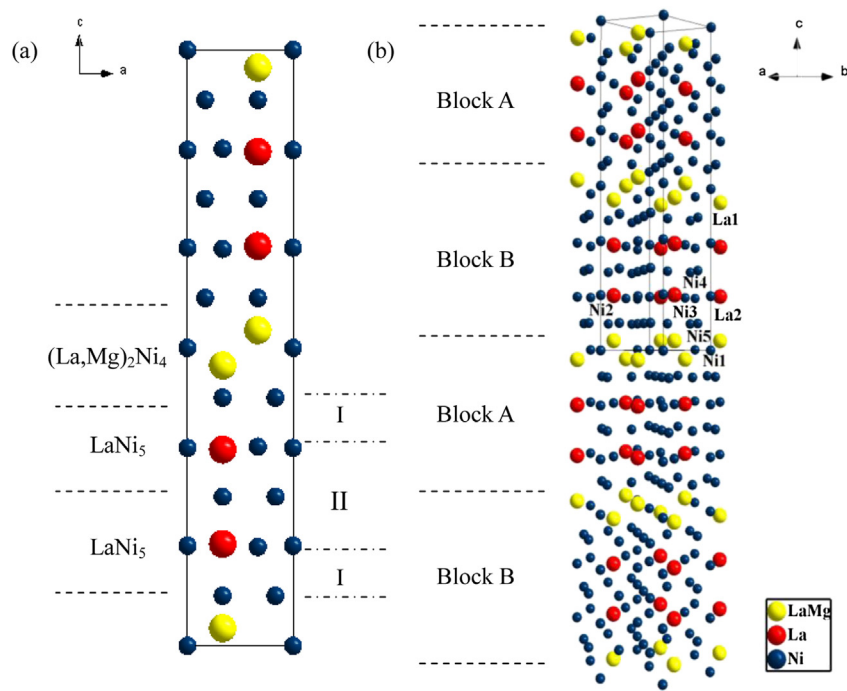


Fig. 3. Structure stacking model of Ce₂Ni₇-type La_{1.6}Mg_{0.4}Ni₇ alloy.

Table 2

Comparison of selected crystallographic parameters for reported Ce₂Ni₇-type La–Ni and La–Mg–Ni alloys.

Parameters	Alloys					
	La ₂ Ni ₇ [1]	La _{1.63} Mg _{0.37} Ni ₇ [2]	La _{1.6} Mg _{0.4} Ni ₇	La _{1.5} Mg _{0.5} Ni ₇ [3]	La _{1.5} Mg _{0.5} Ni ₇ H _{9.3} [3]	La _{1.6} Mg _{0.4} Ni ₇ H _{9.4}
<i>a</i> (Å)	5.058	5.0437	5.0409	5.0285	5.4121	5.4824
<i>c</i> (Å)	24.710	24.319	24.290	24.222	26.589	26.842
<i>V</i> (Å ³)	547.47	536.52	534.53	530.42	674.48	698.69
<i>V</i> _{2AB5} (Å ³)	177.35	177.20	176.58	175.77	221.50	228.57
<i>V</i> _{A2B4} (Å ³)	96.35	91.05	90.69	89.01	115.74	120.78
Δ <i>a/a</i> (%)	–	–0.28	–0.34	–0.58	+7.63	+8.76
Δ <i>c/c</i> (%)	–	–1.54	–1.70	–1.97	+9.77	+10.51
Δ <i>V/V</i> (%)	–	–2.0	–2.4	–3.1	+27.16	+30.71
Δ <i>V</i> _{2AB5} / <i>V</i> _{2AB5} (%)	–	–0.1	–0.4	–0.7	+26.02	+28.71
Δ <i>V</i> _{A2B4} / <i>V</i> _{A2B4} (%)	–	–5.5	–5.9	–7.6	+30.03	+33.18

dots sporadically can be observed due to the oxidation of alloy surface in the preparation process. Fig. 4(b) is the EDS for elemental composition of area A taken from Fig. 4(a). These results indicate that the atomic composition is La_{18.36}Mg_{4.48}Ni_{79.15}, which is also confirmed by ICP with the composition of La_{17.78}Mg_{4.44}Ni_{77.78}.

The selected-area electron diffraction (SAED) pattern with the lower magnified image of the particle confirms that the La_{1.6}Mg_{0.4}Ni₇ crystalline particle is indeed a hexagonal Ce₂Ni₇ type (P6₃/mmc) structure and a single-crystal pattern on the relevant lattice spacing (Fig. 5(a)). The crystal growth direction is along the

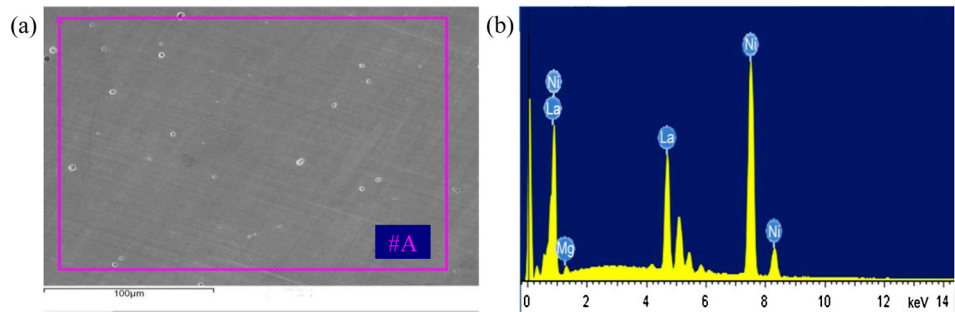


Fig. 4. SEM-EDS analysis of La_{1.6}Mg_{0.4}Ni₇ alloy annealed at 1223 K: (a) SEM backscattering electron image, (b) EDS pattern.

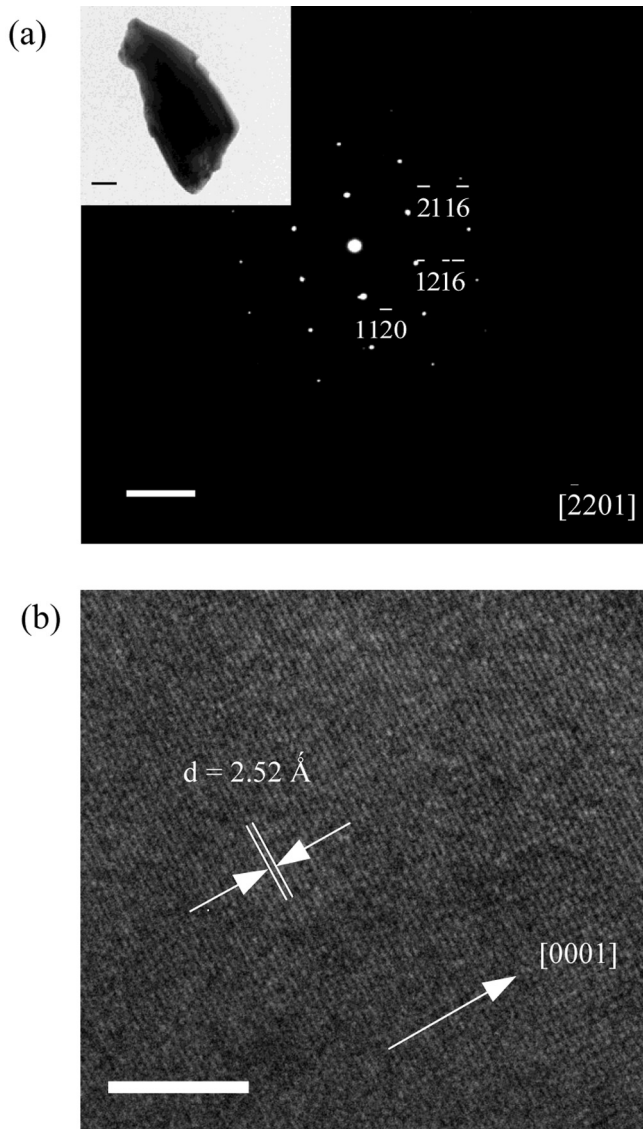


Fig. 5. TEM images of the $\text{La}_{1.6}\text{Mg}_{0.4}\text{Ni}_7$ alloy annealed at 1223 K: (a) the selected-area electron diffraction (SAED) pattern taken along the zone axes of $[\bar{2}201]$ with a low magnified morphology image, (b) high resolution TEM (HRTEM) image.

$[0001]$ orientation and decided by the inter-planar spacing d corresponding to the $[1120]$ plane, as shown in Fig. 5(b).

3.2. P – C isotherm

The P – C isotherms of the Ce_2Ni_7 -type single phase $\text{La}_{1.6}\text{Mg}_{0.4}\text{Ni}_7$ alloy at 298, 323 and 348 K are shown in Fig. 6(a). Each plateau is slightly slope except the relatively flat dehydrogen isotherm at 298 K. The hydrogen absorption plateaus were observed between 0.11 and 1.16 wt.% of hydrogen content at high temperatures (323 and 348 K) and between 0.07 and 1.19 wt.% at 298 K. The increase of temperature from 298 to 348 K causes the elevation of plateau pressures from 0.018 to 0.125 MPa for hydrogen absorption and from 0.0099 to 0.069 MPa for hydrogen desorption.

Based on the equilibrium pressures from the P – C isotherms, the enthalpy change ΔH and entropy change ΔS were calculated to be $-33.4 \text{ kJ mol}^{-1} \text{ H}_2$ and $-193.3 \text{ J (K mol)}^{-1} \text{ H}_2$ for H_2 absorption, and $33.7 \text{ kJ mol}^{-1} \text{ H}_2$ and $195.2 \text{ J (K mol)}^{-1} \text{ H}_2$ for H_2 desorption according to the Van't Hoff plots of the $\text{La}_{1.6}\text{Mg}_{0.4}\text{Ni}_7$ – H system, as

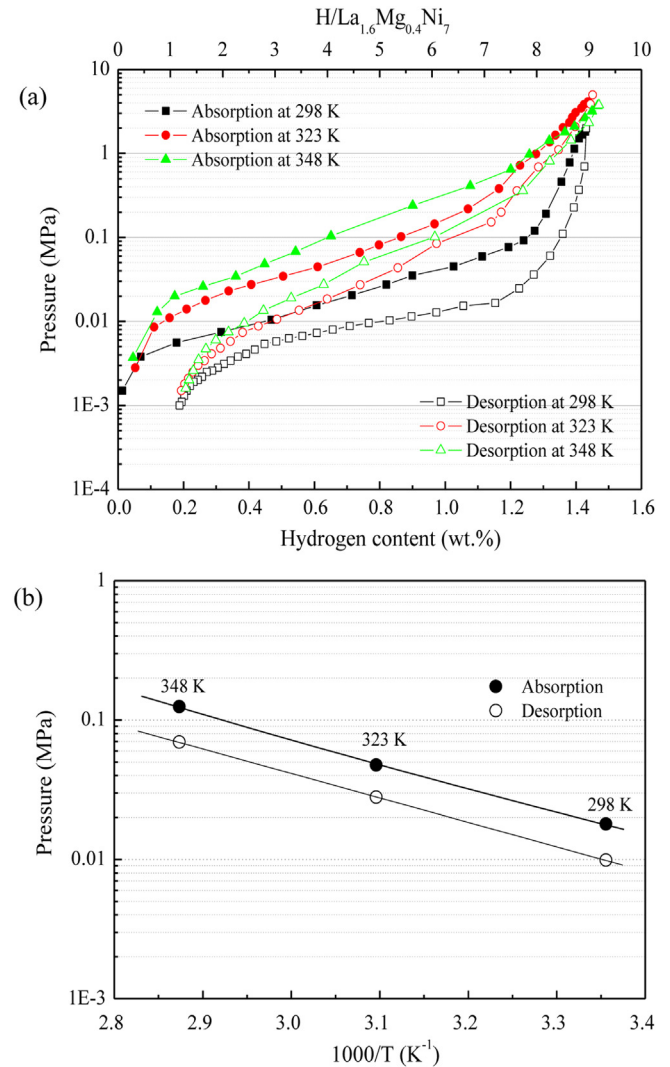


Fig. 6. $\text{La}_{1.6}\text{Mg}_{0.4}\text{Ni}_7$ – H_2 system: (a) P – C isotherms of H_2 absorption and desorption, (b) Van't Hoff plots $\log P_{\text{H}_2}$ vs. $1000/T$.

displayed in Fig. 6(b). The hydrogenated and dehydrogenated enthalpies are $-31.4 \text{ kJ mol}^{-1} \text{ H}_2$ lower but $33.6 \text{ kJ mol}^{-1} \text{ H}_2$ higher than those of $\text{La}_{1.5}\text{Mg}_{0.5}\text{Ni}_7$ – H_2 system [15]. The numbers change to $-32.1 \text{ kJ mol}^{-1} \text{ H}_2$ and $31.5 \text{ kJ mol}^{-1} \text{ H}_2$ for the $\text{La}_4\text{MgNi}_{19}$ – H_2 system [23], indicating both the hydrogen absorption and hydrogen storage stability of $\text{La}_{1.6}\text{Mg}_{0.4}\text{Ni}_7$ alloy are better than those of $\text{La}_{1.5}\text{Mg}_{0.5}\text{Ni}_7$ and $\text{La}_4\text{MgNi}_{19}$ alloys.

The maximum hydrogen capacity reaches 1.43 wt.% under a hydrogen pressure of 2.0 MPa at 298 K, i.e., $\text{H}/\text{La}_{1.6}\text{Mg}_{0.4}\text{Ni}_7 = 9.1$. The consecutive increase of maximum hydrogen capacity is in evidence when temperature rises, achieving 1.47 wt.% at 348 K. This value is similar to that of $\text{La}_{1.5}\text{Mg}_{0.5}\text{Ni}_7$ – H_2 system with reported $\text{H}/\text{La}_{1.5}\text{Mg}_{0.5}\text{Ni}_7 = 9.3$ (1.48 wt.%) under 1.2 MPa at 298 K, but higher than $\text{La}_{1.63}\text{Mg}_{0.37}\text{Ni}_7$ – D system in which $\text{D}/\text{La}_{1.63}\text{Mg}_{0.37}\text{Ni}_7$ is 8.8 under 1 MPa at 353 K. Liao et al. found that the increase of Mg amount in $\text{La}_{1-x}\text{Mg}_x\text{Ni}_3$ ($x \leq 0.67$) led to a gradual decrease in hydrogenation capacity [24], however, this trend was not found in $(\text{La},\text{Mg})_2\text{Ni}_7$ system.

3.3. Crystal structures after hydrogenation and dehydrogenation

Fig. 7(a) and (b) show the Rietveld refinements of XRD patterns of the Ce_2Ni_7 -type single phase of $\text{La}_{1.6}\text{Mg}_{0.4}\text{Ni}_7$ samples after first

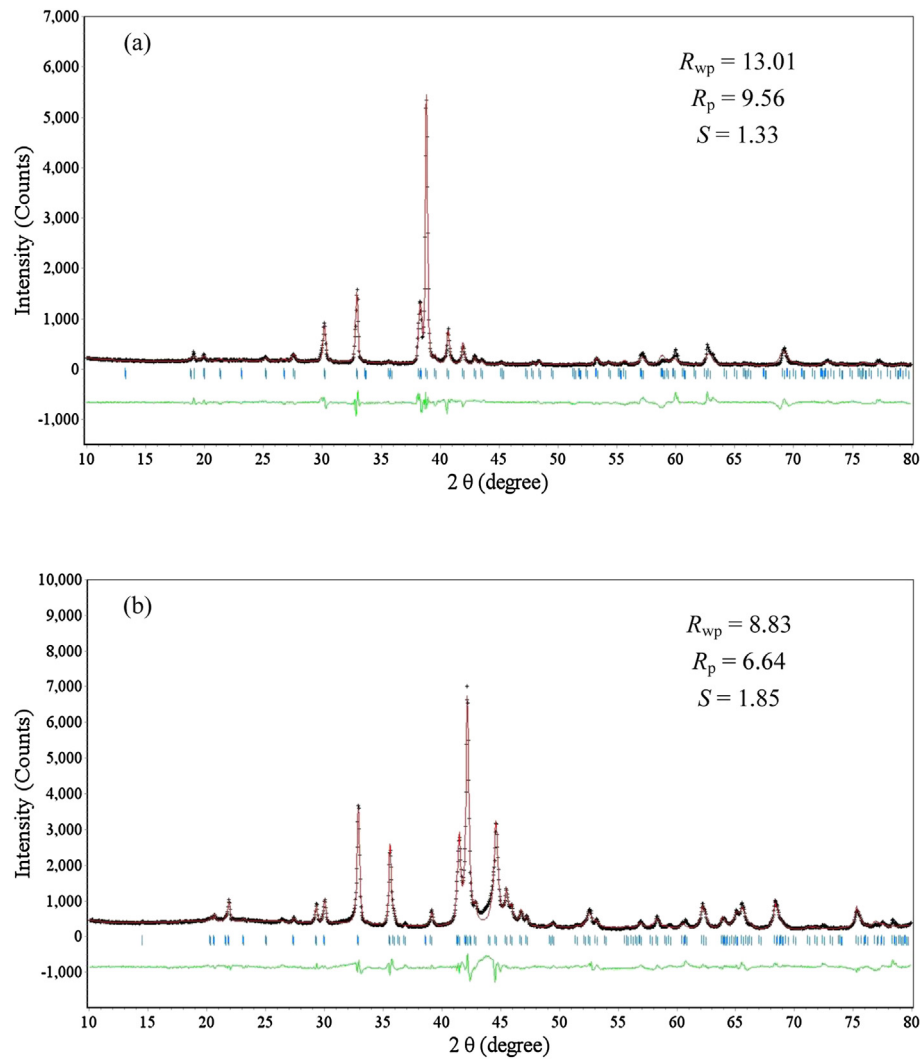


Fig. 7. Rietveld refinements of XRD patterns for Ce₂Ni₇-type La_{1.6}Mg_{0.4}Ni₇: (a) after first hydrogenation, (b) after first dehydrogenation.

full hydrogen absorption and desorption (down to 0.001 MPa). S_0 , S_a and S_d represent the original single phase La_{1.6}Mg_{0.4}Ni₇ sample, the sample after the first full hydrogen absorption and desorption, respectively. Furthermore, the refined lattice parameters a and c are measured to be 5.4824 and 26.842 Å for S_a , and 5.0413 and 24.363 Å for S_d . In La₂Ni₇–H₂ system, two hydride phases were found in the first hydrogen absorption process: La₂Ni₇H_{7.1} with an orthorhombic structure (Pbcn) and La₂Ni₇H_{10.8} with a monoclinic structure (C2/c) [25]. A similar structural change was also observed for Ce₂Ni₇ with a hexagonal structure (P6₃/mmc) turning to an orthorhombic structure (Pmcn) of Ce₂Ni₇D_x [26]. In this study, however, we did not find such structural transitions after the first hydrogenation in Mg containing Ce₂Ni₇-type alloy, and not in other Ce₂Ni₇-type (La,Mg)₂Ni₇ alloys either. We believe that the discrepancy is caused by the occupation of Mg in La1 sites, which stabilizes the Ce₂Ni₇-type structure.

As drawn in Fig. 3(a), each stacking block of Ce₂Ni₇-type structure in La_{1.6}Mg_{0.4}Ni₇ can be divided into three parts: the [La_{1.22}Mg_{0.78}Ni₄] slab, the “outer” [LaNi₅] slab next to the [La_{1.22}Mg_{0.78}Ni₄] slab, and the “inner” [LaNi₅] slab between the two layers of “outer” [LaNi₅] slabs [15]. Phases I and II represent the “outer” and “inner” [LaNi₅] slabs, respectively. The differences between the two types of [AB₅] slabs (I and II) are dependent on the relative spatial sites of the La₂, Ni₂ and Ni₃ atoms (Fig. 3(b)).

Changes of the structural parameters of the unit cell as well as the volumes in the [A₂B₄] slab and the other two types [AB₅] slabs of Ce₂Ni₇-type La_{1.6}Mg_{0.4}Ni₇ after the initial hydrogen absorption and desorption processes are calculated and shown in Table 3.

For S_a sample, the volume expansion corresponds to the amount of hydrogen absorbed by each slab [27]. The volume expansion of each slab in Ce₂Ni₇-type La_{1.6}Mg_{0.4}Ni₇ is in the order of [La_{1.22}Mg_{0.78}Ni₄] > [LaNi₅] II > [LaNi₅] I, indicating that hydrogen atoms are not evenly distributed in [LaNi₅] and [La_{1.22}Mg_{0.78}Ni₄]

Table 3
Expansion (%) of the lattice axes a , c , unit cell volume V , and the volume of the La_{1.22}Mg_{0.78}Ni₄ and LaNi₅ (I and II) slabs from the original sample (S_0) to the first hydrogenated sample (S_a) and the first dehydrogenated sample (S_d).

Sample	S_a	S_d
a	+8.76	+0.01
c	+10.51	+0.30
V	+30.71	+0.31
c (LaNi ₅ I slab)	+8.16	−2.40
c (LaNi ₅ II slab)	+10.73	+3.79
c (La _{1.22} Mg _{0.78} Ni ₄ slab)	+12.59	−0.44
V (LaNi ₅ I slab)	+27.95	−2.37
V (LaNi ₅ II slab)	+30.96	+3.80
V (La _{1.22} Mg _{0.78} Ni ₄ slab)	+33.18	−0.42

slabs. In S_d sample, lattice parameter a does not change, but lattice parameter c and unit cell volume expand by approximately 0.3% compared with S_0 sample, suggesting that the unit cell expands anisotropically along c -axis after dehydrogenation. The $[\text{LaNi}_5]$ II slab volume expands by 3.80%, but the volumes of $[\text{LaNi}_5]$ I and $[\text{La}_{1.22}\text{Mg}_{0.78}\text{Ni}_4]$ slabs shrink by 2.37 and 0.42%, respectively. Residual hydrogen stays in the $[\text{LaNi}_5]$ II slab and leads to the remained expansion. There are three sites for hydrogen atoms to be occupied in $[\text{LaNi}_5]$ II slab: $\text{Ni}_4/4e$, $\text{La}_2\text{Ni}_2/6m$ and $\text{LaNi}_3/12n$, as well as in $\text{LaNi}_5\text{D}_{6.37}$, and four available sites $6h_1$, $6h_2$, $12k_1$ and $24l$ in MgZn_2 -type $[\text{LaMgNi}_4]$ slab [15]. Hydrogen atoms in the CaCu_5 -type Haucke structure are relatively stable while it is completely opposite in the MgZn_2 -type Laves structure with unstable H atoms. Consequently, the initial dehydrogenated pressure of Laves phase is about 1 MPa [28] higher than that of LaNi_5 phase with 0.2 MPa [29], indicating that the hydrogen desorption of the former is easier. However, the desorption plateau (in which α - and β -alloy-H coexist) of the former is more slope compared with the latter one, demonstrating the hydrogen desorption rate in Laves phase is lower than that in LaNi_5 phase. The $[\text{AB}_5]$ and $[\text{A}_2\text{B}_4]$ slabs in Ce_2Ni_7 -type phase possess similar hydrogenation behaviors due to their similar structures. When hydrogen starts to desorb, it first leaves $[\text{A}_2\text{B}_4]$ slab due to the higher desorption plateau, but the gentle tempo makes the platform title upward, as shown in Fig. 6(a). Then $[\text{A}_2\text{B}_4]$ slab contracts by release of hydrogen, and then squeezes the basal plane that is sandwiched between the

$[\text{A}_2\text{B}_4]$ and $[\text{AB}_5]$ I slabs. Meanwhile, the environmental hydrogen pressure atmosphere of $[\text{AB}_5]$ I slab will be lower than $[\text{AB}_5]$ II slab due to the decrease of hydrogen in $[\text{A}_2\text{B}_4]$ slab. The two factors combine to make $[\text{AB}_5]$ I slab release hydrogen prior to $[\text{AB}_5]$ II slab. Hydrogen atoms in $[\text{AB}_5]$ I will soon traverse and finally are released, however, they will stay stable in $[\text{AB}_5]$ slab II due to its structure and restriction of the low rate dehydrogenation of $[\text{A}_2\text{B}_4]$ slab. Hydrogen atoms in $[\text{AB}_5]$ II slab are tied up but they can completely be released in $[\text{A}_2\text{B}_4]$ slabs. Consequently, the residue hydrogen atoms are left in $[\text{AB}_5]$ II slab with expansion of 3.80% and 0.42% contraction to $[\text{A}_2\text{B}_4]$ slab, and $[\text{AB}_5]$ I slab contracts most by 2.37% due to its sandwich structure.

The crystal features of the hydride and dehydride of the $\text{La}_{1.6}\text{Mg}_{0.4}\text{Ni}_7$ alloy with 20 cycles of hydrogenation/dehydrogenation are presented in Fig. 8(a–d). Fig. 8(a) shows the XRD patterns of the hydride and dehydride of the $\text{La}_{1.6}\text{Mg}_{0.4}\text{Ni}_7$ alloy with 20 cycles of hydrogenation/dehydrogenation. Broad peaks were observed, indicating an amorphous tendency that the structures of the two patterns are no longer a Ce_2Ni_7 -type configuration but CaCu_5 -type $\text{LaNi}_5\text{H}_{5.6}$, LaH_3 , MgH_2 and Ni phases for the hydrides, and LaNi_5 and Ni phases for the dehydride. The corresponding SAED patterns of the hydride and dehydride are shown in Fig. 8(b) and (c) with zoom-in morphological images inserted. The morphological images show that all the black crystal particles are surrounding by the gray smog-like matrix, indicating that the crystals are noncrystallized. From the SAED pattern in

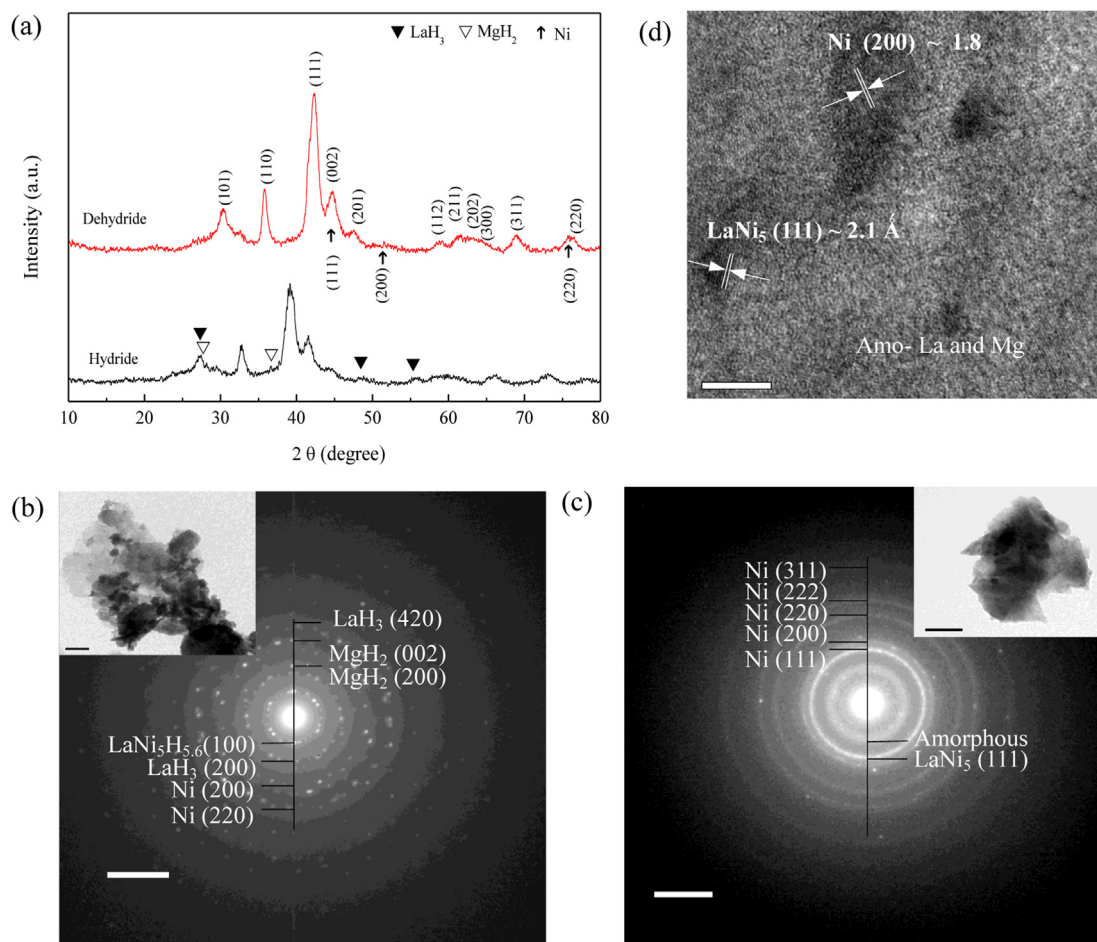
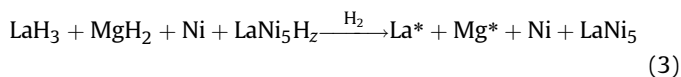
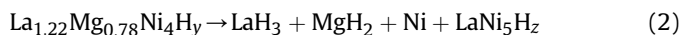
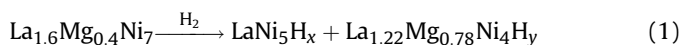


Fig. 8. Ce_2Ni_7 -type $\text{La}_{1.6}\text{Mg}_{0.4}\text{Ni}_7$ alloy: (a) XRD patterns of hydride and dehydride for 20 cycles, (b) SAED pattern of hydride for 20 cycles with a lower magnified morphology image, (c) SAED pattern of dehydride for 20 cycles with a lower magnified morphology image, (d) HRTEM image of dehydride for 20 cycles.

Fig. 8(b), we can recognize that these particles and matrixes consist of hydrides $\text{LaNi}_5\text{H}_{5.6}$, LaH_3 and MgH_2 with Ni, which is consistent with the XRD results. The strong diffraction spots nestled on weak diffused continuous diffraction rings indicate that these hydrides form their own nanocrystalline aggregates. For the dehydride after 20 cycles, the SAED pattern was found to be amorphous structures with sharp multiple rings of polycrystalline state. The multiple rings can be indexed by LaNi_5 with hexagonal (space group $P6/mmm$, no. 191) and Ni with cubic (space group $Fm-3m$, no. 225) structures as shown in Fig. 8(c). It should be noted that these features are also well revealed in the HRTEM image in Fig. 8(d), in which the spheroidal nanocrystalline LaNi_5 and Ni with roughly ~ 10 nm diameters are embraced by amorphous phases La and Mg.

The conversion of the Ce_2Ni_7 -type phase to the nanocrystalline CaCu_5 -type and Ni phases after several hydrogenation/dehydrogenation cycles can be explained by violent reaction between $[\text{A}_2\text{B}_4]$ slab of the Ce_2Ni_7 -type structure and hydrogen, as indicated by the great change of slab volume of 33.6% between S_d and S_a samples. After several cycles, the reaction results in the destruction of the Laves structure. The precipitation of LaNi_5 and Ni exist in crystal forms, but La and Mg atoms are in a disordered amorphous phase after dehydrogenation of LaH_3 and MgH_2 . Simultaneously, some $[\text{AB}_5]$ slabs may keep intact structure and reconstruct CaCu_5 -type phase. Therefore, LaNi_5 and Ni phase peaks can be detected in XRD patterns. The similar decomposition of Laves phase was also observed in LaNi_2 [30] and DyNi_2 [19]. However, the phase decomposition phenomenon does not appear in the very first cycle, with the possible reason that the change of structural strain caused by the lattice expansion during hydrogenation and dehydrogenation may be within the elastic deformation range and the energy from exothermic hydrogenation process is lower than the decomposition energy of $[\text{A}_2\text{B}_4]$ slab after expansion. Therefore, the $[\text{A}_2\text{B}_4]$ slab remains originally after the first hydrogenation. While, repetitive lattice expansion of $[\text{A}_2\text{B}_4]$ slab may reduce strain and energy between the La/Mg–Ni, La(Mg)–La(Mg) or Ni–Ni bonds after several cycling hydrogenation/dehydrogenation, which leads to the decomposition energy of $[\text{A}_2\text{B}_4]$ slab lower than the energy from exothermic hydrogenation process at this point, resulting in the decomposition of $[\text{A}_2\text{B}_4]$ slab. As a result, the $[\text{La}_{1.22}\text{Mg}_{0.78}\text{Ni}_4\text{H}_x]$ slab decomposed into $\text{LaNi}_5\text{H}_{5.6}$, LaH_3 , MgH_2 and Ni during the hydrogenated process after several hydrogenation/dehydrogenation cycles, as shown in expression (1) and (2). The disproportionated alteration process of the Ce_2Ni_7 -type $\text{La}_{1.6}\text{Mg}_{0.4}\text{Ni}_7$ alloy to the amorphous phase La and Mg, as well as noncrystalline LaNi_5 and Ni phases after several hydrogenation/dehydrogenation, can be described as hydrogenation-induced phase decomposition, one hydrogen-induced amorphization (HIA) phenomenon, as shown below:



* existing as an amorphous state finally.

3.4. Maximum discharge capacity and cyclic stability

As shown in Fig. 9, the Ce_2Ni_7 -type single phase $\text{La}_{1.6}\text{Mg}_{0.4}\text{Ni}_7$ alloy electrode exhibits 400 mAh g^{-1} , top over all the other alloys. The effect of annealing treatment is homogeneous for the alloying

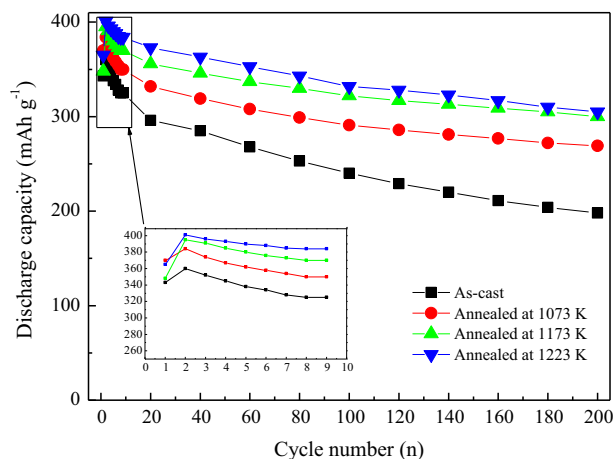


Fig. 9. Discharge capacity vs. cycle number of $\text{La}_{1.6}\text{Mg}_{0.4}\text{Ni}_7$ alloy.

components by solid diffusion. With the elevation of the annealing temperature, the homogenization degree increases because of the acceleration of atom diffusion velocity. This concept represents structural transformation through the peritectic reactions at the macro level. Therefore, CaCu_5 -, $\text{Ce}_5\text{Co}_{19}$ - and Gd_2Co_7 -type phases are gradually homogenized after annealing treatment, obtaining the Ce_2Ni_7 -type single phase $\text{La}_{1.6}\text{Mg}_{0.4}\text{Ni}_7$. Additionally, in the process of annealing, the lattice strain decreases and the grain size becomes finer, both facilitating the compositional homogeneity. Consequently, the maximum discharge capacity of the single phase is the most advantageous one.

Fig. 10 shows the discharge curves (the second cycle) of the alloy electrodes. Obviously, each curve has a wide discharge potential plateau based on the oxidation of desorbed hydrogen from the hydride, especially for the single phase alloy. Moreover, the discharge plateau of the alloys shifts towards a more positive potential as increase of annealing temperature, which the middle-discharge potential decreases to -0.8906 V for single phase alloy from -0.8753 V for alloy annealed at 1123 K .

The cycling capacity retention rate for an electrode after n charge/discharge cycles is expressed as $S_n (\%) = C_n/C_{\max} \times 100\%$ (where C_{\max} is the maximum discharge capacity and C_n is the discharge capacity at the n cycles). The single phase alloy has obviously enhanced cycle life compared with other multiphase

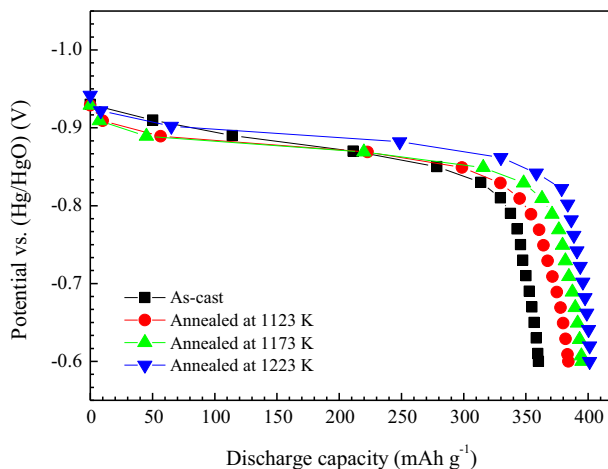


Fig. 10. Discharge curves of the as-cast and annealed $\text{La}_{1.6}\text{Mg}_{0.4}\text{Ni}_7$ alloys at discharge density of 60 mA g^{-1} (298 K).

alloys, which the S_{100} and S_{200} of the Ce_2Ni_7 -type single phase $\text{La}_{1.6}\text{Mg}_{0.4}\text{Ni}_7$ alloy is 84.2 and 76.1%. In the repetitive charge/discharge cycles, the phase decomposition of the Ce_2Ni_7 -type phase also occurs due to the hydrogen absorption/desorption process. On the one hand, the precipitating amorphous phases of La and Mg easily turn into $\text{La}(\text{OH})_3$ and $\text{Mg}(\text{OH})_2$ when the fresh areas are exposed to the alkali solution after the pulverization of the alloy. One the other hand, after the phase decomposition, LaNi_5 phase acts as hydrogen absorption/desorption material rather than the Ce_2Ni_7 -type phase, contributing to the decrease of the discharge capacity of the alloy. For other multiphase alloys, the decomposition of each superlattice phase also happens due to structural changes of the Mg-containing slab. However, the structural changes of each phase are out of sync, meaning that the stabilities of these phases are different, with stressful strain inside the alloy particles increased correspondingly. Then the speed of pulverization and the corrosion are boosted which give rise to worse cycle life of multiphase alloys electrodes than that of single phase alloy electrode. The cycling stability of the Ce_2Ni_7 -type single phase $\text{La}_{1.6}\text{Mg}_{0.4}\text{Ni}_7$ alloy obtained by annealing treatment has been improved without decreasing the maximum discharge capacity within an affordable cost.

4. Conclusions

A Ce_2Ni_7 -type (hexagonal 2H) single phase $\text{La}_{1.6}\text{Mg}_{0.4}\text{Ni}_7$ alloy was prepared by annealing the induction-melted alloys at 1223 K for 12 h. After hydrogenation, the volume expansion of the three kinds of slabs of $[\text{La}_{1.22}\text{Mg}_{0.78}\text{Ni}_4]$, $[\text{LaNi}_5]$ II (inner) and $[\text{LaNi}_5]$ I (outer) in the Ce_2Ni_7 -type phase structure decreases gradually. After dehydrogenation, the residual hydrogen is in $[\text{LaNi}_5]$ II slab owing to the restraint of slow dehydrogenation rate of $[\text{La}_{1.22}\text{Mg}_{0.78}\text{Ni}_4]$ slab after hydrogen desorption of $[\text{LaNi}_5]$ I slab. The consecutive volume change, of which volume change rate of the Mg-containing slab is larger than those of $[\text{LaNi}_5]$ (I and II) slabs, ultimately causing the decomposition of Ce_2Ni_7 -type phase to amorphous phases La and Mg, nanocrystalline Ni and CaCu_5 -type LaNi_5 phases after 20 cycles of hydrogenation/dehydrogenation, leading to the decay of electrochemical discharge capacity. Thermodynamic studies show that enthalpy changes are $-33.4 \text{ kJ mol}^{-1} \text{ H}_2$ and $33.7 \text{ kJ mol}^{-1} \text{ H}_2$ for H_2 absorption and desorption, respectively. The maximum discharge capacity of the single phase alloy electrode is up to 401 mAh g^{-1} , and the cycling stability of the alloy electrode prepared by annealing treatment is superior.

Enhancement of the structural stability of Mg-containing slabs within a superlattice structure after hydrogenation/dehydrogenation is the fundamental solution to strengthen the phase structure stability and improve the electrochemical properties of the superlattice structure alloy as the battery electrode materials.

Acknowledgments

This work (research) was financially supported by the National Natural Science Foundation of China (NOS. 51171165 and 21303157), the Natural Science Foundation of Hebei Province (NOS. B2012203027 and B2012203104), Scientific Research Foundation for the Returned Overseas Chinese Scholars of Hebei Province (20100501) and the China Postdoctoral Science Foundation Project (2013M541201).

References

- [1] K. Young, T. Ouchi, B. Huang, J. Power Sources 248 (2014) 147–153.
- [2] C.C. Nwakwuo, T. Holm, R.V. Denys, W. Hu, J.P. Maehlen, J.K. Solberg, V.A. Yartys, J. Alloys Compd. 555 (2013) 201–208.
- [3] T. Takasaki, K. Nishimura, M. Saito, H. Fukunaga, T. Iwaki, T. Sakai, J. Alloys Compd. 580 (Suppl. 1) (2013) S378–S381.
- [4] K. Young, J. Nei, Materials 6 (2013) 4574–4608.
- [5] Y. Liu, H. Pan, M. Gao, Q. Wang, J. Mater. Chem. 21 (2011) 4743–4755.
- [6] X. Zhao, L. Ma, Int. J. Hydrogen Energy 34 (2009) 4788–4796.
- [7] M. Tiha, K. Khaldi, S. Boussami, N. Fenineche, O. El-Kedim, H. Mathlouthi, J. Lamloumi, J. Solid State Electrochem. 18 (2013) 577–593.
- [8] R.V. Denys, V.A. Yartys, J. Alloys Compd. 509 (Suppl. 2) (2011) S540–S548.
- [9] L. Zhang, S.M. Han, Y. Li, J.J. Liu, J.L. Zhang, J.D. Wang, S.Q. Yang, Int. J. Hydrogen Energy 38 (2013) 10431–10437.
- [10] W.K. Hu, R.V. Denys, C.C. Nwakwuo, T. Holm, J.P. Maehlen, J.K. Solberg, V.A. Yartys, Electrochim. Acta 96 (2013) 27–33.
- [11] J. Nakamura, K. Iwase, H. Hayakawa, Y. Nakamura, E. Akiba, J. Phys. Chem. C 113 (2009) 5853–5859.
- [12] J. Balej, Int. J. Hydrogen Energy 10 (1985) 365–374.
- [13] F.L. Zhang, Y.C. Luo, J.P. Chen, R.X. Yan, J.H. Chen, J. Alloys Compd. 430 (2007) 302–307.
- [14] F.L. Zhang, Y.C. Luo, D.H. Wang, R.X. Yan, L. Kang, J.H. Chen, J. Alloys Compd. 439 (2007) 181–188.
- [15] R.V. Denys, A.B. Riabov, V.A. Yartys, M. Sato, R.G. Delaplane, J. Solid State Chem. 181 (2008) 812–821.
- [16] M.N. Guzik, B.C. Hauback, K. Yvon, J. Solid State Chem. 186 (2012) 9–16.
- [17] J. Zhang, F. Fang, S. Zheng, J. Zhu, G. Chen, D. Sun, M. Latroche, A. Percheron-Guégan, J. Power Sources 172 (2007) 446–450.
- [18] K. Ishikawa, N. Ogasawara, K. Aoki, J. Alloys Compd. 404–406 (2005) 599–603.
- [19] H.W. Li, K. Ishikawa, K. Aoki, J. Alloys Compd. 399 (2005) 69–77.
- [20] Y. Liu, Y. Cao, L. Huang, M. Gao, H. Pan, J. Alloys Compd. 509 (2011) 675–686.
- [21] X.B. Zhang, D.Z. Sun, W.Y. Yin, Y.J. Chai, M.S. Zhao, J. Power Sources 154 (2006) 290–297.
- [22] Y. Li, D. Han, S.M. Han, X.L. Zhu, L. Hu, Z. Zhang, Y.W. Liu, Int. J. Hydrogen Energy 34 (2009) 1399–1404.
- [23] Q.G. Zhang, M.H. Fang, T.Z. Si, F. Fang, D.L. Sun, L.Z. Ouyang, M. Zhu, J. Phys. Chem. C 114 (2010) 11686–11692.
- [24] B. Liao, Y.Q. Lei, G.L. Lu, L.X. Chen, H.G. Pan, Q.D. Wang, J. Alloys Compd. 356–357 (2003) 746–749.
- [25] K. Iwase, K. Sakaki, Y. Nakamura, E. Akiba, Inorg. Chem. 49 (2010) 8763–8768.
- [26] R.V. Denys, V.A. Yartys, M. Sato, A.B. Riabov, R.G. Delaplane, J. Solid State Chem. 180 (2007) 2566–2576.
- [27] K. Iwase, N. Terashita, K. Mori, S. Tsunokake, T. Ishigaki, Int. J. Hydrogen Energy 37 (2012) 18095–18100.
- [28] K. Young, T. Ouchi, J. Koch, M.A. Fetcenko, J. Alloys Compd. 510 (2012) 97–106.
- [29] H. Senoh, N. Takeichi, T. Kiyobayashi, H. Tanaka, H.T. Takeshita, T. Oishi, N. Kuriyama, J. Alloys Compd. 47–50 (2005) 404–406.
- [30] U.I. Chung, J.Y. Lee, J. Non-Cryst. Solids 110 (1989) 203–210.